Toward quantitative three-dimensional microvascular networks segmentation with multiview light-sheet fluorescence microscopy

Pol Kennel,[a] Lise Teyssedre,[b] Julien Colombelli,[c] and Franck Plouraboué[a,*]

[a]Toulouse University, CNRS, INPT, UPS, Institute of Fluid Mechanics of Toulouse, Toulouse, France
[b]ITAV, USR 3505, National Center of Scientific Research, Toulouse, France
[c]Advanced Digital Microscopy Core Facility, Institute for Research in Biomedicine (IRB Barcelona), Barcelona Institute of Science and Technology, Barcelona, Spain

Abstract. Three-dimensional (3-D) large-scale imaging of microvascular networks is of interest in various areas of biology and medicine related to structural, functional, developmental, and pathological issues. Light-sheet fluorescence microscopy (LSFM) techniques are rapidly spreading and are now on the way to offer operational solutions for large-scale tissue imaging. This contribution describes how reliable vessel segmentation can be handled from LSFM data in very large tissue volumes using a suitable image analysis workflow. Since capillaries are tubular objects of a few microns scale radius, they represent challenging structures to reliably reconstruct without distortion and artifacts. We provide a systematic analysis of multiview deconvolution image processing workflow to control and evaluate the accuracy of the reconstructed vascular network using various low to high level, metrics. We show that even if low-level structural metrics are sensitive to isotropic imaging enhancement provided by a larger number of views, functional high-level metrics, including perfusion permeability, are less sensitive. Hence, combining deconvolution and registration onto a few number of views appears sufficient for a reliable quantitative 3-D vessel segmentation for their possible use for perfusion modeling. [DOI: 10.1117/1.JBO.23.8.086002]

Keywords: light sheet; multiview imaging; vascular network; microvasculature; permeability.

1 Introduction

The perspective of imaging tubular structures associated with fibers,[1] vascular structures,[2] or roots[3] is relevant in many biomedical contexts: development, tissue remodeling, physiology, etc. However, even if many studies have considered imaging local vessels, very few have tackled the complete reconstruction of very large volumes.[4–9] One motivation for aiming to perform such microvascular networks reconstruction is the modeling of blood perfusion[7–9] to decipher supracellular level organization from the analysis of the microvascular network[7,10] and to gain a global understanding of tissue structure/function physiology as opposed to local analysis at the cellular scale. Vascular structures provide nonlocal (graph-based) structural information, directly relevant to perfusion and metabolic exchanges, for which a tissue-scale computerized analysis can bring significant understanding to tissue functions. Going from fibers/tubular shapes in images to vascular tubes necessitates skeletonization processing. Many skeletonization methods have been proposed (cf., Refs. 11 and 12 for reviews) based on various techniques such as vessel enhancement filters, region-growing approaches, active contour centerline-based methods, stochastic frameworks using particle filters, and Markov marked point processes. Among these, homotopy preserving skeletonization methods provide very satisfactory results[10,13,14] when applied to isotropic voxels imaging such as x-ray tomography. Nevertheless, when dealing with nonisotropic imaging resulting from optical microscopy, one has to reconsider the entire set of workflow associated with image treatments to evaluate the reliability and sensitivity of the vessel's segmentation.

One significant difficulty of LSFM is controlling illumination light scattering and absorption, whose effects can immensely degrade image quality in depth and widely depend on the shaping of the light sheet. Many techniques have been developed to compensate for laser light-sheet scattering, such as resonating mirror,[15] multiview deconvolution,[16,17] structured illumination,[18] and adaptive optics.[19] Another important issue in LSFM is isotropic imaging because isotropic voxels are of tremendous assistance for reliable quantification and segmentation of spherical (e.g., cells and nucleus) or cylindrical (e.g., vessels and fibers) objects. Light-sheet fluorescence microscopy (LSFM) is an emerging and rapidly growing field where many variants are currently developed.[20,21] Currently, major efforts are applied to image large samples, in areas ranging from multicellular organoids/spheroids,[17] whole organisms at the embryo level,[22,23] whole mount mammalian tissues,[1] and plants.[20,24] The segmentation of large vascular networks resulting from light-sheet imaging has rarely been performed and, to our knowledge, the quantification of the image analysis workflow accuracy associated with LSFM three-dimensional (3-D)-images applied to the blood vessel challenge has not been studied yet.

The aim of this contribution is to analyze the impact and benefits of multiview deconvolution LSFM for a reliable and quantitative 3-D reconstruction of fiber/vascular networks. We describe how large-field-of-view multiview LSFM imaging and deconvolution, performed on images acquired at low

*Address all correspondence to: Franck Plouraboué, E-mail: franck.plouraboue@imft.fr

magnification, can be used to provide highly accurate reconstruction and segmentation of the entire vascular network of large tissue volumes. We focused our attention primarily on addressing the aspects related to multiview deconvolution and quality assessment of the resulting vascular segmentation.

2 Materials and Methods

The imaging and analysis workflow follows steps given in Fig. 1(d). Tissue preparation and LSFM instrument are described in Sec. 2.1. Appendices B and C provide details about the registration and deconvolution steps.

2.1 *Tissue Preparation and LSFM Imaging*

The mice studied were anesthetized by intraperitoneal injection of ketamine/xylazine mix. Then, an *in vivo* retro-orbital lectin injection was performed to achieve proper vessel labeling (rhodamine labeled griffonia simplicifolia lectin I, RL-1102 from Vectorlabs). Before tissue removal, animals were perfused intracardially with 4% paraformaldehyde solution. Tissue was then removed, oriented, and postfixed overnight, sunk in phosphate buffer saline. Afterward, tissue was embedded in 1% agarose before being dehydrated by ethanol then cleared by incubation in benzyl alcohol-benzyl benzoate solution (BABB, 1:2 vol:vol ratio) (Sigma-Aldrich). The sample is shown in Fig. 1(a). All experiments were carried out in compliance with European Community Guidelines (2010/63/UE) and approved by the French Ethics Committee. Experiments were performed on 6- to 8-week-old male C57BL/6J mice (Harlan Laboratories) on a 12-h light/dark cycle with free access to food and water. Cleared samples were imaged on a custom LSFM system based on $f = 50$-mm cylindrical lens illumination with a 561-nm laser (Oxxius, France) and a horizontal macroscope detection with a 7-mm slit aperture to control the geometry of the light sheet (thickness and flatness). The resulting thickness T of the light sheet at the waist varied from 5 to 50 μm according to the slit aperture. For the data sets of this paper, T was set to a full-width at half-maximum (FWHM) of about 20 μm to conserve homogeneous illumination over the largest field of view (FOV) at the lowest magnification (i.e., 1.2×) with a Macroscope (Nikon AZ100M), a 2× air objective lens, and an eightfold zoom factor. The anisotropy of detection is shown in Figs. 1(e)–1(g). The resolution of the microscope was determine empirically by estimating the smallest vessel diameters (near diffraction limit) by Gaussian fit. Imaging cleared samples were performed through 2-mm-wall glass polished cuvettes. Rotation of the sample was performed by acting on the agarose block embedding the sample with a driving rotation stage (M116-DGH, Physik Instrumente, Karlsruhe, Germany). Detection was performed with 50-nm bandpass filters and a CCD camera (ORCA-R2, Hamamatsu, Japan). Figures 1(i)–1(k) show a typical vascular network image resulting from the imaging system at 6.72× with a voxel size of $0.967 \times 0.967 \times 1.34$ μm^3.

To perform resolution measurements in BABB, we used subdiffraction 1-μm silica fluorescently labeled beads (DiagNano DNG-L026, CD: creative diagnostics, New York), merged in agarose blocks prior to clearing in BABB.

2.2 *Multiview Registration and Deconvolution*

Appendices B and C provide more details about registration and deconvolution steps referenced in Fig. 1(d). In short, for registration, we use rigid transforms based on normalized cross correlation (NCC) with accurate multiscale and optimization tuning using the elastix library.[25] For deconvolution, we use the Richardson–Lucy (RL) method, which has proven appropriate for multiview deconvolution.[23,26–28] Segmentation step five and quality analysis step six [cf., Fig. 1(d)] are discussed in Secs. 2.3 and 2.5, respectively. Section 2.4 provides details about the manual segmentation performed to obtain ground truth reference vascular networks.

2.3 *Vessel Segmentation and Skeletonization*

Deconvolved images are thresholded and the resulting binary images are then used for network extraction. The spatial graph representing the vascular network is built up according to the vectorization of the binary image as described in Ref. 29. The vessels' center lines are extracted with an appropriate homotopy preserving skeletonization method[30] used and described in Ref. 29. (Avizo© FEI software has been used for visualization only, not for any of the hereby described image treatment.) Our experience with homotopy preserving skeletonization[30] (a special class of region-growing approach) has provided reliable and robust results.[10,14] The graph $G = (V, E)$ is then created, where V, the set of nodes, is extracted from the branching-voxel and end-voxel, and E, the set of edges, is extracted between connected node-voxels of the vessel skeleton. An edge is composed of a chain of center line voxels comprised between two nodes. In the following, we will refer to segment and segment element instead of edges and center line voxels as shown in Fig. 2(a). Vessel radii are estimated following Ref. 14: for each segment element and node, a sphere is expanded until 10% of its volume is left outside the vessel shape in the binary image. Figure 1(b) shows the network extracted from Fig. 1(a) with tubular-like visualization in Avizo© FEI software.

2.4 *Data Sets*

We manually segmented three samples of 128^3 voxels to assess segmentation accuracy. The manual segmentation consists of building a binary image, which can then be vectorized as described in Sec. 2.3. Each sample is composed of about 300 segments, 300 nodes, and 4000 segment elements. Sample #1 of our ground truth data set is presented in Appendix D [Fig. 8(a)]. We also created a 128^3 voxels artificial network, presented in Appendix D [Fig. 8(c)], based on our knowledge of the vascular properties of the analyzed tissue, i.e., using statistics described in Sec. 3.4. This synthetic network is used to simulate the estimated convolution artifact of the imaging system as well as a controlled level of degradation as shown in Appendix D [Fig. 8(c)].

2.5 *Quality Evaluation*

We have defined several metrics to appreciate the quality of the extracted graph network based on ground truth data sets. These metrics are elaborated to quantify accuracy from low- to high-level structural properties of the vascular network. The details of the metrics are given in Appendix A.

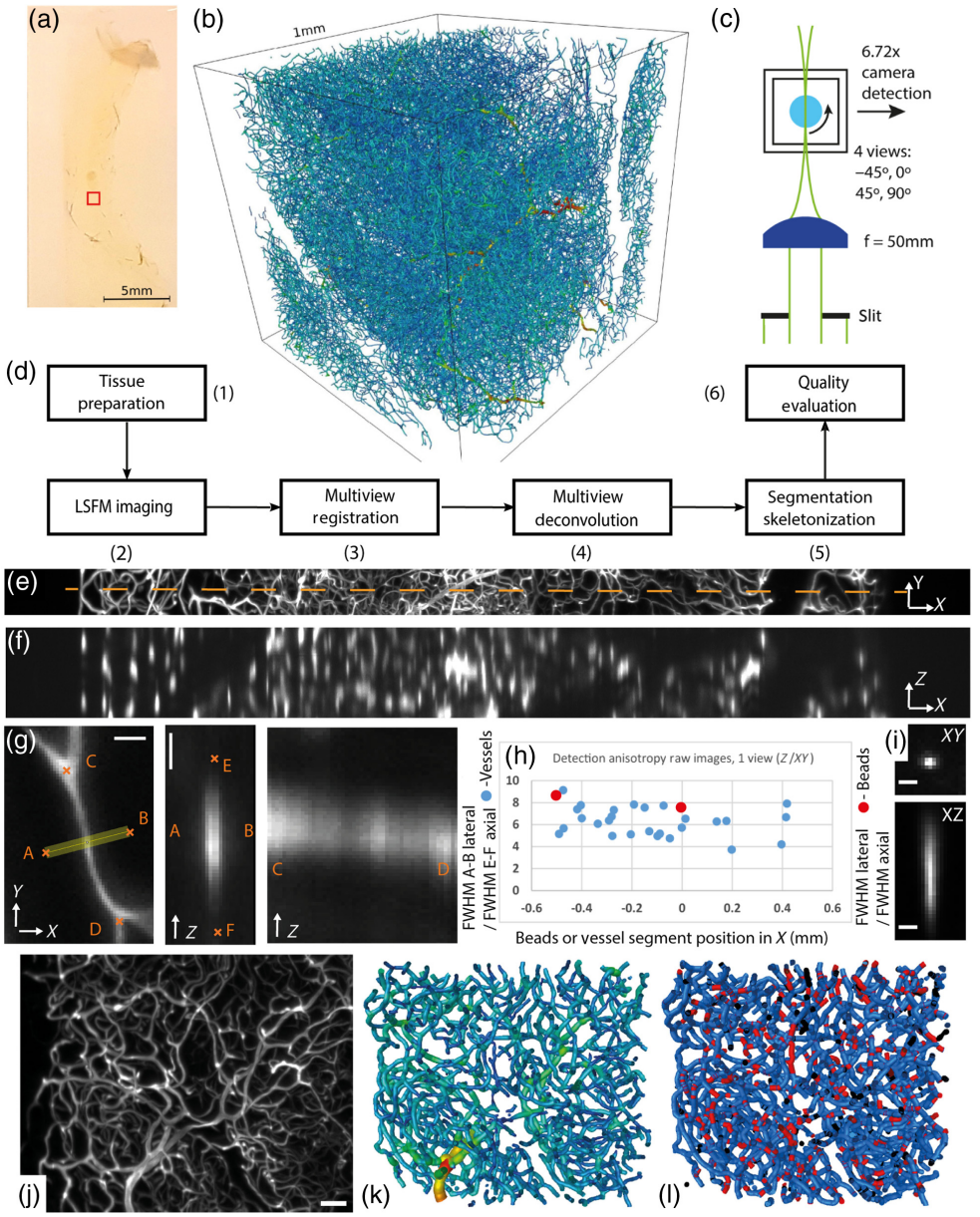

Fig. 1 (a) Photography of a cleared mice inguinal adipose tissue. The red square indicates where LSFM imaging has been performed. (b) Illustration of a 1-mm^3 segmented and reconstructed vascular network sample corresponding to the square region shown in (a). The network is composed of about 42,000 segments, 22,000 bifurcations, and 1,063,000 segment elements. Segments are scaled and colored according to their estimated diameter (from cold color for small ones to hot color for large ones). (c) Schematic representation of the LSFM instrument showing, not at scale, the glass chamber, the Agarose block (in cyan) where the sample is embedded, the cylindrical lens (blue), and the slit to adjust the light-sheet geometry. (d) Flowchart of the imaging, postprocessing, and analysis workflow. (e) Maximum intensity projection (150-μm depth) of a small portion at full XY width (1 mm) of one view. (f) $X - Z$ profile of the centerline (dashed) in (e). (g) $X - Y$ and axial profile of a small vessel oriented in $X - Y$, axial profiles are represented perpendicular (A–B) and along the vessel axis (C–D). (h) Ratio of the Gaussian FWHM of $n = 27$ vessels distributed across the width of the data sets (blue data points) to show consistent light-sheet geometry across the width of the image yielding an average isotropy of detection $X - Y$ versus Z of about 6.25. The same ratio is measured on fluorescent beads and yields (red data points) 7.9 ($n = 10$) in the center and 8.8 ($n = 10$) on the edge of the image. Scale bars (g) and (h) 10 μm. (i) Image of a glass fluorescent bead laterally and axially, scale bar μm. (j) Closer view maximum intensity projection of an XY-plane of 100 μm Z-depth; scale bar: 40 μm. (k) The vascular network visualized with tubular structures in Avizo (FEI) software extracted from (a) with four-views reconstruction; the color scale encodes vessel diameter. (l) Similarly, the vascular network extracted and compared for four-views and one-view data sets: shared segment elements are in blue, black segment elements are specific to the one-view-based network, and red segment elements are specific to the four-views-based network. The four-views network contains several segments elements important for the topology and the permeability (in red), which are not present in the one-view network; moreover, the one-view network contains artifact segment elements (in black), which do not contribute to the permeability of the vascular network.

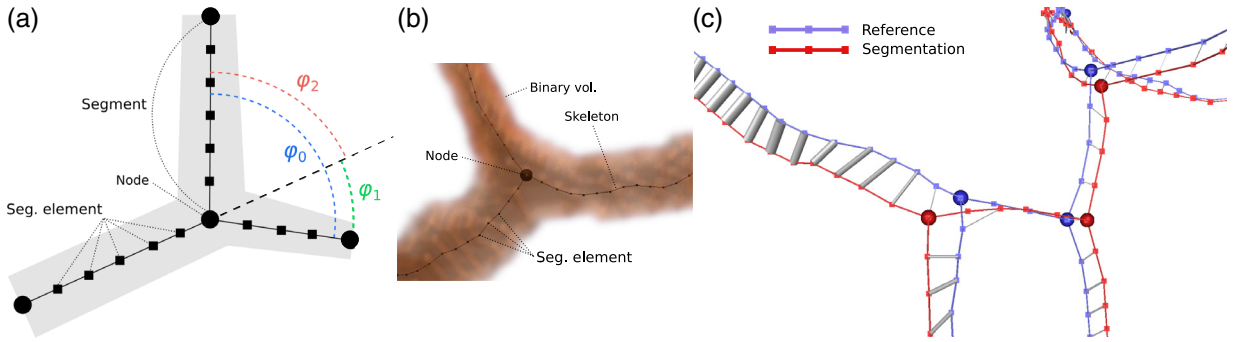

Fig. 2 (a) Network notations and bifurcation angles definitions. (b) Illustration within one bifurcation of the skeletonization result. (c) Illustration of the comparison between two networks: the reference graph (in blue) is composed of segment element (small bullets) paired with the ones of the segmented graph in red. The pairing is materialized with gray cylinders, the diameter of which is scaled according to the associated pairing error using the minimum cost flow algorithm.

3 Results

We performed light-sheet imaging of a fluorescently stained blood vessels network in cleared mouse adipose tissue, as shown in Fig. 1.

Two complementary strategies are possible for imaging vascular networks in large tissue volumes with LSFM: (i) using an axially confined light sheet (i.e., very thin) with tiled imaging of small FOVs or (ii) using an axially "thicker" light sheet at a large FOV. Depending on the detection system and its numerical aperture (NA), lateral resolution may be acceptable over a wide range of magnification to opt for the lowest number of tiles or FOVs, thereby avoiding extensive mosaic stitching. However, the axial extent of the light sheet required to homogeneously illuminate a large FOV may increase the anisotropy of detection in the *XY*-sheet plane versus the *Z*-direction, perpendicularly to the sheet plane. Higher magnification with thinner light-sheet illumination will bring more isotropic detection and would be a preferred instrumental choice. Nevertheless 3-D stitching may be challenging on whole mount organs, both for the intensity discontinuity between neighbors' positions and for colinearity of light sheet. The required *XY*-movement may bring troublesome axial discontinuities in the data set. Ideally, imaging at the lowest magnification would save in acquisition complexity, time, and data storage. In the present contribution, we focus our interest on the image processing of the second strategy, for which multiview deconvolution can be used for the enhancement of image quality in large image data sets.[16,26]

3.1 *Multiview Deconvolution*

Figure 3(b) shows the resulting deconvolved images with the tuned parameter for the n-views configuration ($n \in [1:4]$). The intensity profiles plotted in Fig. 3(c) show how the voxel isotropy is improved considering that the transverse section of the vessel, where the profiles were extracted, should be circular. Note that the one-view deconvolution configuration delivers only an intermediate recovery of the *Z*-isotropy. Also, Fig. 3(c) (first, third, and fourth plots) displays one example of nonperfect centering of profiles following registration, which is further discussed at the end of Sec. 4. Finally, Figs. 3(b) and 3(c) show that the TV regularization perfectly prepares images for segmentation by favoring high gradient and homogeneous regions, so a simple thresholding of the intensity then provides an appropriate vessel segmentation.

3.2 *Accuracy on Ground Truth Data*

Precision–recall curves for voxel matching and segment-element matching are plotted in Figs. 4(a) and 4(b) for the n-views configurations. Points of the curves are obtained by applying various threshold values to the deconvolved images resulting in binary images and then vascular graphs (Sec. 2.3). An ideal case would be a precision [i.e., the ratio of false positives (FP)] equal to the recall (i.e., the ratio of misses) and equal to 1 (i.e., no FP and no misses). From the two metrics, it is clear that four views outperform all other configurations in any cases. However, three views and two views provide close results, much better than the one-view configuration. Similar conclusions can be drawn from other ground truth data, showing a significant improvement from the $n = 1$ view to a larger number of views ($n > 1$).

Figure 4(c) shows the complete set of accuracy metrics resulting from the segmentation of ground truth samples #1, #2, and #3 and for n-views configurations ($n \in [1,4]$). For the three low-level metrics [voxel matching (F-score vox.), segment-element matching (F-score el.), and diameter error] as well as for the graph similarity, a clear trend stands out for the three samples: the best score, resp. the lowest error, is found for the four-views configurations and decreases, resp. increases, for the three views, two views, and finally reach the lowest score, resp. highest error, for the one-view configurations. Hence, here again, the one view ($n = 1$) provides much lower results than $n > 1$ regarding these metrics. It is interesting to mention that the diameter error from ground truth is, respectively, found equal to 35%, resp. 24%, for $n = 1$, resp. $n = 4$. This could appear quite accurate, but one has to bear in mind that perfusion is very sensitive to local vessel diameter, as given by the fourth power dependence of the local conductance. This is why the conductance error from ground truth is found much higher in whole sets. This is also why an accurate representation of vessels is a key methodological point for modeling tissues since a reliable quantitative estimate of conductance properties is a prerequisite for modeling. However, high-level accuracy metrics, i.e., the conductance and the permeability error, reveal a more mitigated trend. Concerning the conductance, the four-views configuration provided, again, the lowest error compared with the others for sample #2, which is not

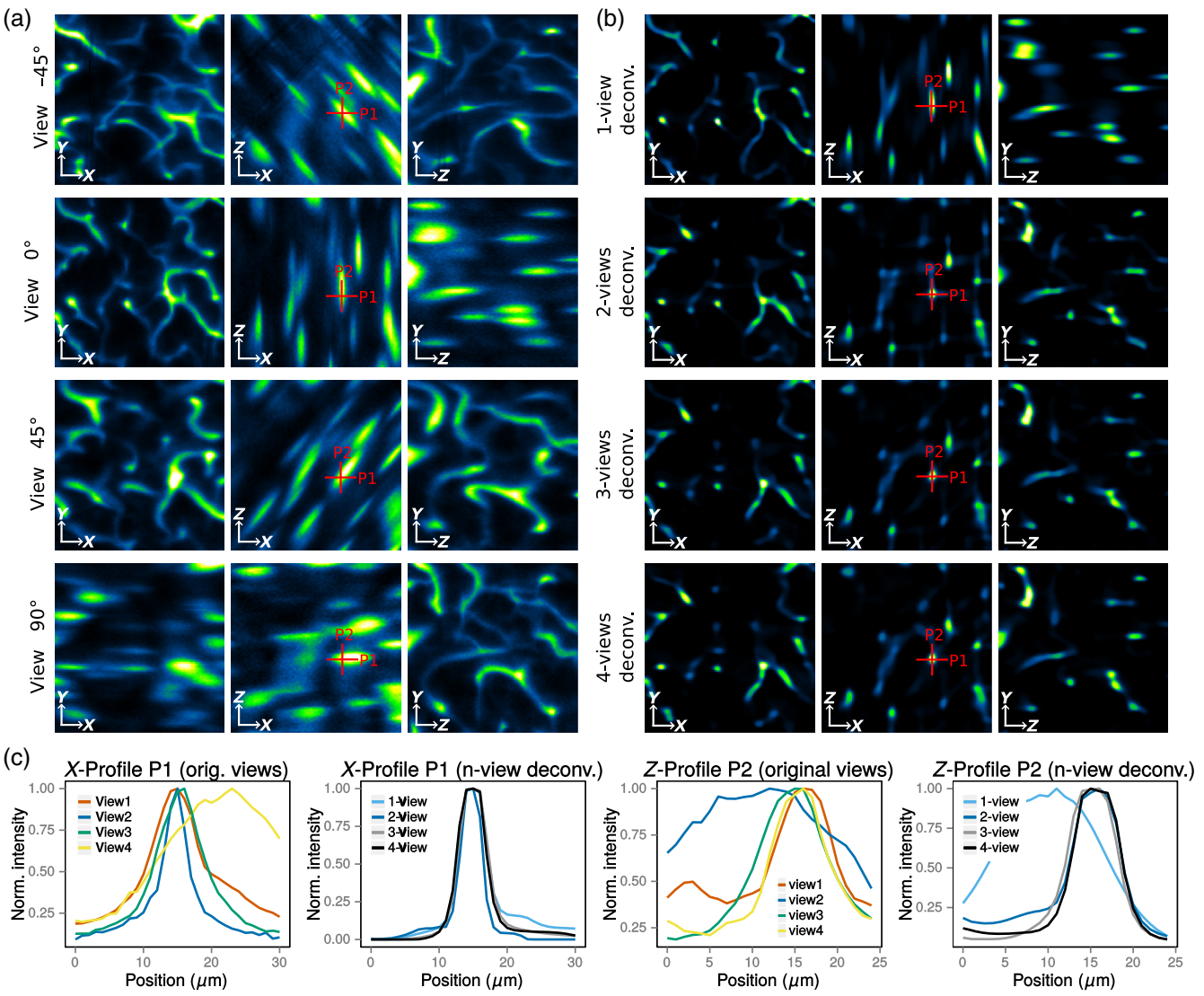

Fig. 3 Improvement of the vascular network imaging isotropy from using multiview deconvolution. (a) Illustration of raw isotropic 128 μm^2 orthogonal plans extracted at the same spot with four different views (imaging angles equal to −45, 0, 45, and 90 deg). Views at −45, 45, and 90 deg are registered based on view at 0 deg. (b) Illustration of the corresponding multiview deconvolved isotropic 128-μm^2 orthogonal plans obtained according to n-view configurations with $n = 1$ (using view at 0 deg), $n = 2$ (using views at 0 and 90 deg), $n = 3$ (using views 0, 45, and 90 deg), and $n = 4$ (using views −45, 0, 45, and 90 deg), RLTV iteration = 25, and TV = 0.01 (cf., Appendix C for more information). (c) X (P1) and Z (P2) intensity profiles extracted at the red-cross spot (XZ-plans) from the raw images [for the four angles in (a)] and the n-view deconvolved images [with n from 1 to 4 in (b)].

the case for samples #1 and #3, where no clear trend emerges. Concerning the permeability error, it is interesting to note that the lowest error results from the four-views configuration only for sample #3 (with a clear trend), whereas it remains unstable for samples #1 and #2.

3.3 *Synthetic Data*

We take advantage of the synthetic network to monitor controlled degradation and evaluate how n-views perform on the network extraction regarding to the six accuracy metrics in the presence of increasing additive Gaussian noise [illustrated in Appendix D, Fig. 8(c)] and Poissonian noise. Figure 5(a) shows the n-views configuration score/error evolution for each metric according to Gaussian noise level [peak signal-to-noise ratio (PSNR)]. Similar results can be found in Fig. 5(b) for Poissonian noise distribution.

Again, a clear trend stands out for the three low-level metrics (the voxel matching F-score, the segment-element matching F-score, and the diameter error) as well as the high-level graph similarity: the four-views configuration outperforms the three others with highest score/similarity and resp. lowest error, whichever noise level applied. Similarly, three views outperform two views, and two views outperform one-view configuration. However, even if the conductance metric shows a similar hierarchy at a low noise level, it does not display a clear trend any more for noisy images. Concerning the permeability error, even if the curves are noisy, we found a similar trend as previously observed (cf., Sec. 3.2) for real data. One view gives the highest error and the three other configurations give much lower, but

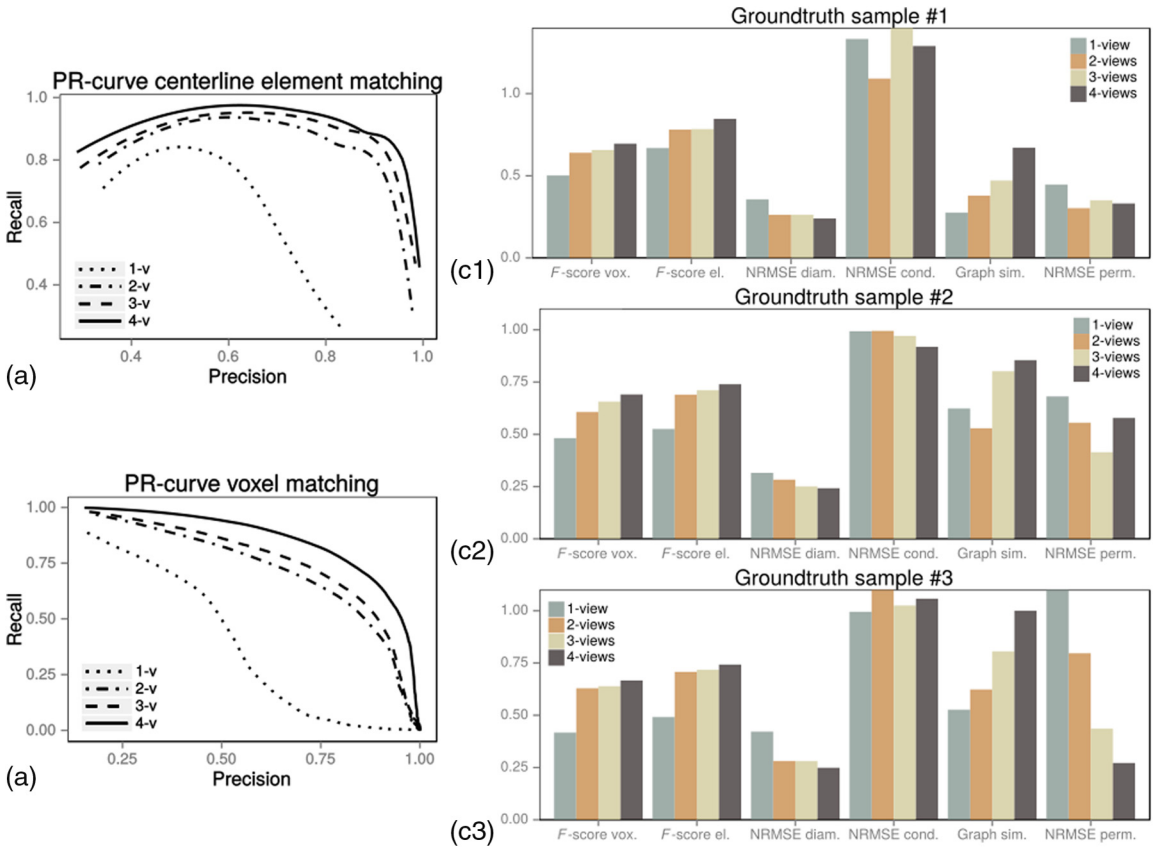

Fig. 4 Left column: precision–recall (cf., Appendix A.1 for definitions) curves for (a) voxels matching and (b) segment-elements matching resulting from segmentation and network extraction, with optimal deconvolution parameters, of ground truth data set #1. Right column: comparison of several accuracy metrics resulting from our network segmentation workflow on three ground truth data sets according to *n*-views reconstructions. Parameters used (cf., Appendix C for more information): (c1) #1 RLTV it. = 30 TV = 0.001, (c2) #2 RLTV it. = 35 TV = 0.001, and (c3) #3 RLTV it. = 60 TV = 0.001.

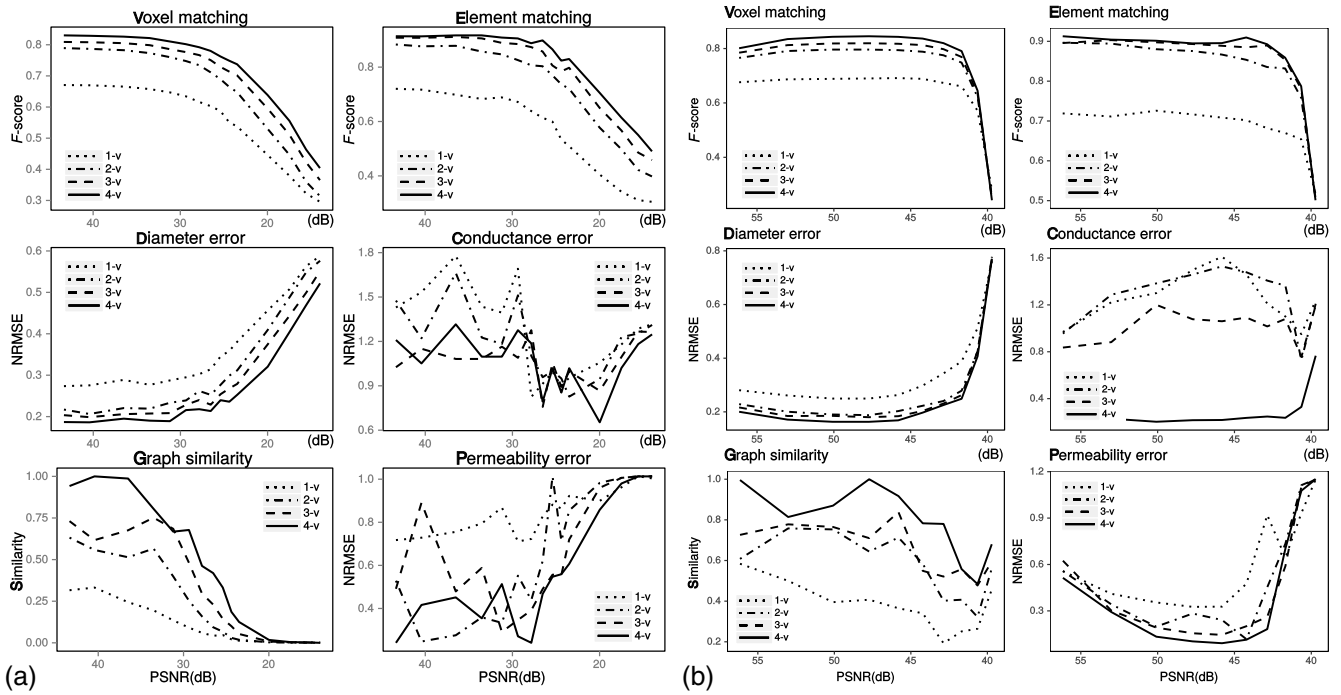

Fig. 5 Sensitivity of vascular network extraction to additive (a) Gaussian noise and (b) Poissonian noise evaluated using six different accuracy metrics on our synthetic network with *n*-views reconstructions ($n \in [1,4]$) (cf., Appendix A for more information about metrics).

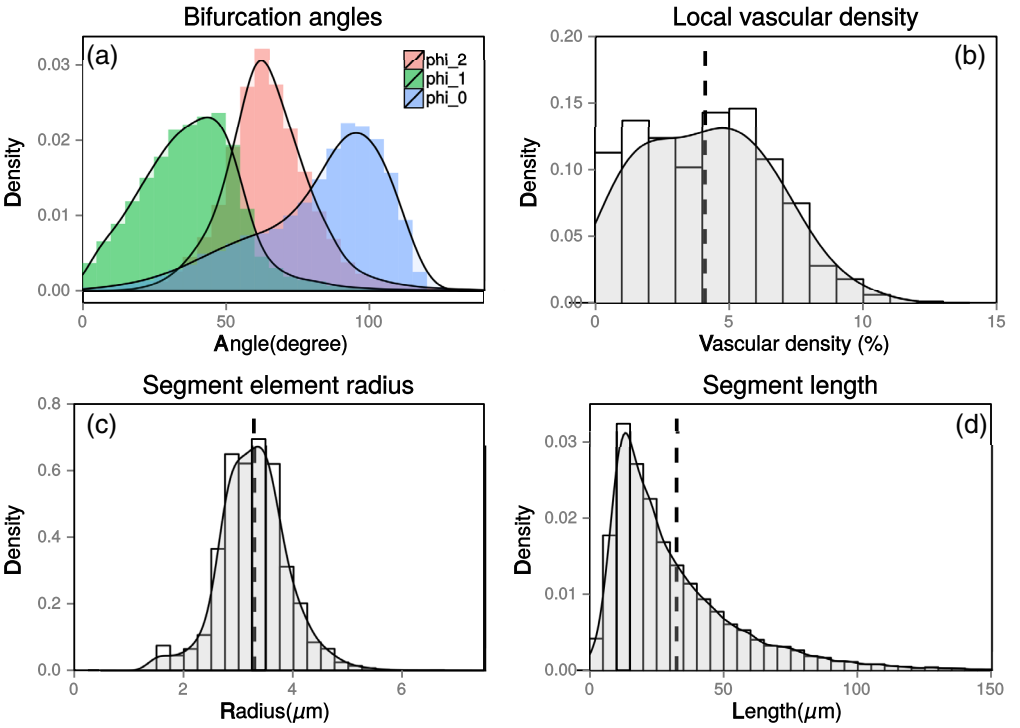

Fig. 6 Statistics of interest calculated on the vascular network extracted from the large mice tissue sample presented Fig. 1(b). (a) Bifurcation angles according to convention presented Figs. 2(a) and 2(b) relative local vascular volumic density (volume fraction of vessels) computed into 100-μm voxels, (c) radius of segment elements, and (d) segment length. Vertical dashed lines represent mean values.

quite similar, errors with a slight advantage for four views. Hence, it is interesting to crop-up the statement that $n > 1$ views are generally much better than one view for vascular network segmentation with a variable advantage of increasing the number of view n.

3.4 *Vascular Network Analysis of Biological Tissue*

When applied at a large scale, the hereby proposed workflow allows the extraction of important structural properties of vascular networks. Figure 1(b) shows the vectorization of a 1-mm^3 subarea of the vascular network of the inguinal adipose tissue in mice. It reveals a particularly high vascular density [quantified in Fig. 6(b)] compared with other tissues such as brain[14] or muscles. Figure 6 also shows characteristic bifurcation angles according to the convention defined in Fig. 2, as well as the segment length and segment-element radius distributions. Further statistics of interest, including several related to blood microcirculation in the tissue, are provided in Appendix G.

4 Discussion

Optical imaging of large-scale volumes is not easily achievable with conventional optical microscopy. For high-resolution fluorescence data collection, confocal microscopy is still the gold standard. However, its ability to image in very large volumes will suffer drastic axial resolution degradation together with the working distance of the lens, which is required to target a specific depth. In general, the deeper the target is, the lower the NA is and, hence, the lower the axial resolution is. 3-D deconvolution techniques may somehow recover part of this resolution degradation; however, the typical deterioration of signal-to-noise ratio (SNR) at acute depth will not play in favor of this aim. Multiphoton microscopy, on the other hand, is typically limited to 1 mm in depth for *in vivo* experiments, and, even if sample clearing can improve this value, low NA lenses drastically reduce the efficiency of excitation of the technique. On the contrary, the accepted advantages of LSFM are to enable large working distances and high SNR and to offer sample mounting solutions (e.g., sample rotation) that are not accessible in conventional microscopy (e.g., confocal microscopy).

Here, we performed light-sheet imaging of a fluorescently stained blood vessels network in cleared mouse adipose tissue with enhanced anisotropic illumination (i.e., much worse axially) to probe the benefit for vessel segmentation of multiview fusion with deconvolution at low magnification range, and thereby show that high-accuracy blood vessel imaging can be performed without stringent conditions on the need for acquisition of tiled mosaics.

We estimate theoretically that the ratio between the objective lens lateral resolution (about 1.83 μm calculated for a 6.72× magnification, in air, with an estimated NA of 0.2 and classical equation for full lateral extent 0.61× wavelength/NA) and the light-sheet axial extent (set experimentally and measured in air to have a FWHM of about 20 μm, cf., Sec. 2) gives an anisotropy factor of about 9.15. We confirmed this factor experimentally by reporting a characterization of optical resolution with glass beads, yielding from 7.9 to 8.8 [Fig. 1(i)]. Of note, we used glass fluorescent beads to enable imaging in BABB, providing a solution to the well-known problem of latex/polymer beads, which dissolve in this corrosive clearing medium. Finally, we empirically estimate this factor by measuring in the $X - Y$ and Z diameters of the smallest vessels in our raw data sets to be around 6.25 ± -1.3 μm [cf., Fig. 1(h)],

consistently lower because the smallest blood vessels are not subdiffraction objects for this range of magnification.

We were able to show that this factor can be reduced by multiview fusion to yield restored data with an anisotropy factor, i.e., the ratio between axial and lateral resolution, measured closer to 1 [as shown in Fig. 3(c)] even with only two views.

The aim of this contribution is to analyze and evaluate how multiview deconvolution improves the voxel isotropy in 3-D LSFM images for large-scale vascular network extraction. Vascular networks are extremely complex 3-D objects, for which an accurate evaluation of local structural properties is relevant to biological function. Hence, it is important to provide a systematic comparison of the influence of the multiview deconvolution steps and parameters on the subsequent reconstruction precision. Furthermore, the capabilities enabled by recent 3-D LSFM images at the centimeter scale open the road for the exploration of very large tissue volumes, for which a large light-sheet axial extent helps to acquire amounts of data. Our approach, therefore, consisted of working at low magnification to probe the ability to restore highly anisotropic illumination conditions with multiview deconvolution.

In conditions that are experimentally simple to set (at low magnification with air lenses), the potential for image improvement by multiview postprocessing is much larger than at high magnification as the starting anisotropy of *XY*-detection versus *Z* illumination (i.e., light-sheet thickness) is greater, therefore, potentially simplifying the image acquisition procedure. Hence, there is a need for the evaluation of multiview deconvolution numerical costs and benefits for segmentation of large data/volume analysis.

We investigated six different metrics of interest for the analysis of low- to high-level structural properties of vascular networks. Using various ground truth data, we systematically quantified how structural, geometrical, and topological ingredients of vascular vessels are retrieved. First, we found that low-level metrics related to voxel, segment element, and diameter display a clear hierarchical quality response with the number n of views, i.e., four views > three views > two views > one view. These results confirm the interest of multiview deconvolution procedures as they permit reaching high-confidence scores, as shown by *PR* curves of Figs. 4(a) and 4(b). Second, the results given by high-level metrics, especially the permeability, are found to be much less sensitive to the number of views. It shows a decreasing improvement, which could already be observed for low-level metrics in Figs. 4(a) and 4(b). This observation is related to the functional role of vascular networks. Even if, as previously mentioned, small structural local information, e.g., vessel diameters, are important to estimate accurately, they are not everywhere crucial to blood perfusion. When integrated into the network complexity, some vascular segments might not play an important role for perfusion [see Fig. 1(k), the segment difference between one view and four views segmentation]. This is why we found that a 100% error in conductance can translate into a 30% error only in permeability. Also, more interestingly, the progressing quality estimation of high-level metrics given in Fig. 4(c) does not show a clear hierarchical quality response when $n > 1$. Since both computational and memory cost increase as $O(n)$, it is interesting to note that, above $n = 2$, perfusion prediction resulting from multiview deconvolution might poorly improve from increasing the number of views. This trend is confirmed when considering progressive degradation in a synthetic network, shown in Fig. 5. In noisy situations, even low-level metrics display a much larger improvement from $n = 1$ to $n = 2$ than in a further number of view refinements.

The relevance of the presented segmentation workflow is shown in Fig. 6, where various vascular structural parameters have been reported on the analyzed fat tissue. The vessel radius histogram [Fig. 6(c)] displays a bell-shape Gaussian like curve, the mode of which corresponds to a capillary diameter of 7 μm, close to what can be found in brain.[14] The vessel length distribution [Fig. 6(d)] displays a Poissonian like behavior, whose mean length equal to 35 μm is two times shorter than the one found in brain.[14] This feature illustrates the specificity of fat tissue where adipocytes are tightly vascularized, such that vascular segment length is comparable with their half perimeter. Furthermore, vascular volume fraction displays an average 4%, comparable with other tissues (e.g., brain and muscle) with distribution tails reaching values as large as 10%, as shown in Fig. 6(b). Finally, Fig. 6(a) shows the histogram of orientation angles as defined in Fig. 2(a). The orientation angle in red ϕ_2 displays a symmetrical distribution as opposed to the two other angles.[31]

Finally, let us now provide some elements for the usefulness and future extensions of the presented results. Since the exposed test cases (data, ground truth, and C++ code) are provided as supplementary material (supplementary materials data and code are available at: https://drive.google.com/file/d/1evXmG_x7TzL2yoqWa23qA7iJpWSjdZsF/view?usp=sharing), this contribution, using state-of-the-art processing, gives a first step toward quantitative vascular segmentation from LSFM imaging. Specific new methods associated with the image processing workflow, i.e., registration,[32] deconvolution, segmentation,[33] and vectorization, might be interesting to explore in the future since they might help to improve the recovery of vascular properties. A detailed discussion of such possible extensions is obviously beyond the scope of this study. However, considering the registration step, we have explored the possibility of using nonrigid B-spline-based transformation.[25] Such nonrigid deformations require very careful parameter setting and are difficult to configure to reach a perfect alignment of views for each vessel, even considering local deformations sized to the vessel scale. Despite our efforts, we were not able to improve registration, while, at the same time, the computational cost was significantly increased.

5 Conclusion

We analyze the quantitative segmentation of large microvascular networks from multiview LSFM images. Combining suitable multiview deconvolution and registration procedures, we addressed the question of vessel accurate segmentation and vascular network reliable 3-D reconstruction. We showed the benefit of increasing the number of angular views on image-based and structural metrics, confirming the convergence toward isotropic vessel reconstruction. However, considering higher-level metrics, associated with the network topology, lead us to temper the need for a large number of views. Using more than two views does not provide better results on perfusion oriented metrics. The presented results represent the first systematic quantitative evaluation of LSFM postprocessing workflow for reliable vascular network reconstruction. Knowing how much gain could be expected from a very large 3-D images data set and heavy posttreatment computation is of practical interest for

future research. This is especially true for image-based quantitative modeling.

Finally, it is interesting to mention that, even if we mainly restrict our analysis to a cubic millimeter volume of tissue, the applicability of the imaging procedure has a much wider potential. As a matter of fact, the analyzed region is situated inside a much bigger layer into which the light-sheet penetrates (see Fig. 1). Hence, the range of accessible imaged volume is much wider, at least for high-quality clearing. Combining LSFM with a suitable image posttreatment workflow shows potential for centimeter tissue-scale analysis of vascular structures, at micron resolution, a perspective that deserves further investigation and effort.

Appendix A: Metrics Definitions

A.1 Raw Level

We first compare the reference network $I_{\text{ref.}}$ and the segmentation results $I_{\text{seg.}}$ at the raster level on binary images by counting matching voxels using a classical precision/recall measurement. We defined $F\text{-score}_{\text{vox.}} = 2PR/(P+R) \in [0;1]$ with precision $P = \text{TP}/(\text{TP}+\text{FP})$, recall $R = \text{TP}/(\text{TP}+\text{FN})$, true positives (TP), false positives (FP), and false negatives (FN).

A.2 Segment-Element Level

The vascular graph representation allows the measurement of error/score at the level of vascular segments and/or segment elements from the evaluation of matching to a reference segmented graph. The segment-elements level of this matching requires a pairing procedure. For this, we consider the correspondence between segment elements (i.e., pairing) a weighted bipartite graph matching problem. Following Ref. 34, we address this assignment using a minimum cost flow algorithm defining the cost function as the Euclidean distance between elements. From only considering pairs lower than 5 μm apart, we perform the accuracy calculation between each eligible pair. The resulting pairing is shown in Fig. 2(b). We then consider $F\text{-score}_{\text{elem.}}$ using same precision/recall measurement as in Appendix A.1, but obviously considering TP, FP, and TN among the sets of suitable graph segment elements and nodes.

Paired segment elements allow us to compute an error on vessel diameters. We defined a diameter error between graph G_1 and G_2 (say G_1 is the ground truth graph and G_2 a segmented graph) as the normalized root mean square error (NRMSE)

$$\text{NRMSE}_{\text{diam.}}(G_1, G_2) = \frac{1}{d_{1m}} \sum_{i \in P} \left[\sqrt{(d_{1i} - d_{2i})^2} \right], \tag{1}$$

where (e_{1i}, e_{2i}) is the i'th pair of elements from G_1 and G_2, (d_{1i}, d_{2i}) is the corresponding diameters, and d_{1m} is the mean diameter of elements from G_1.

A.3 Segment Level

At the segment level, we consider the error associated with the hydraulic conductance of each vascular segment for the blood to flow from one bifurcation to the next one. This hydraulic conductance is related to the ease, for a given blood pressure to drive perfusion. We refer to the classical definition, e.g., given in Ref. 9, for which conductance c of a vessel segment of length L is given by

$$c = \frac{\pi}{128} \left(\sum\nolimits_{i \in L} \frac{\mu_i}{d_i^4} \right)^{-1}, \tag{2}$$

where d_i is the diameter associated with the i'th segment element, where blood has viscosity μ_i. Since not all elements of a reference segment are paired with elements of a segmented graph, we defined the NRMSE related to conductance only for the paired elements, which is thus a pseudoconductance error, by

$$\text{NRMSE}_c(G_1, G_2) = \frac{1}{c_{1m}} \sum_{s \in E_1} e_c(E_{1s}, G_2), \tag{3}$$

where c_{1m} is the mean conductance of segments E_1 of G_1 and

$$e_c(E_{1s}, G_2) = \sum_{i \in P_s} \sqrt{\left(\frac{1}{d_{1i}^4} - \frac{1}{d_{2i}^4} \right)^2}, \tag{4}$$

where $\mu_i = 1$, P_s are the paired elements of E_{1s} with elements of G_2, and thus d_{1i} and d_{2i} are the associated diameters pair in G_1 and G_2.

A.4 Topological Level

We would like to quantify the topological proximity of segmented vascular networks regarding ground truth with a well-defined metric. For this, we consider a graph similarity measurement developed for pattern recognition and widely used in many computer vision tasks, as well as in graph matching and graph clustering.[35,36] Graph similarity is a difficult task especially when one needs to gauge similarity without explicit correspondence between nodes and edges, as needed here, although we were able to pair segment elements. The main idea is to use spectral graph theory to embed a graph in a Riemannian manifold and to use the curvature embedding as the appropriate invariant property to be compared from one graph to another. Further details of this graph similarity can be found in Appendix E.

A.5 Permeability Level

Finally, the most high-level metric that we consider is concerned with the macroscopic transport properties of the microvascular network: its permeability. This quantity is used to describe the ability of a complex vascular network to perfuse a given blood flux proportionally to the applied pressure difference. Hence, it defines some intrinsic transport coefficient, almost independently of the blood properties (a more accurate discussion is beyond the scope of this contribution[9]). Since the essential biological role of vascular network is to perfuse blood, comparing the transport properties of our segmented networks regarding ground truth is interesting not only from the biological viewpoint but also methodologically since this permeability integrates many structural properties, already present in the previously considered metrics, into a clear functional perfusion property.

Using the network model described in Refs. 9 and 10 for flow transport, we computed perfusion flow into three different

directions denoted p_x, p_y, and p_z. Further explanations about transport model can be found in Appendix F. We defined the relative permeability error as

$$\mathrm{NRMSE}_{\mathrm{perm.}}(G_1, G_2) = \frac{1}{p_{1m}} \sum_{i \in \{x,y,z\}} \sqrt{(p_{1i} - p_{2i})^2}, \qquad (5)$$

where p_{1m} is the mean permeability of G_1 over the three directions and p_{1i} and p_{2i} are the blood fluxes associated in a particular direction for graph networks G_1 and G_2.

Appendix B: Multiview Registration

Before registration, each image, acquired with a different rotation angle, is interpolated in the Z-direction, so voxels match an isotropic dimension of 0.967 μm width. The bead-based registration protocol[16] is not suited to the biological purpose that we pursue since beads are challenging to insert and stabilize homogeneously in the space inside large tissues. Furthermore, the combination of beads and clearing agents is not always compatible, and solvent-based clearing methods, which may provide the best clearing results, may indeed compromise both fluorescence and structural integrity of commonly used polymer beads. In this study, since we opt for a low z-resolution, extracting salient points for point-based registration techniques gives poor results. Even if subsampled data give an approximate registration, high-resolution registration was not possible since no correspondence exists between salient points extracted at high resolution. For this reason, we opt for a rigid registration based on NCC with accurate multiscale and optimization tuning using the elastix library.[25] The registration follows a two-step procedure: (i) a Y-rotation is applied to each view according to the known angle of acquisition, for every view to become almost aligned and (ii) an affine transformation is performed to register each view onto the same view. A typical four-views registration sample is presented in Appendix D [Fig. 8(b)], where the XZ-plane is shown and the artifacts of each view are visible through a cross-like shape of transversal vessel slices. We performed the registration of the supplementary material data set provided for registration (4×512^3 voxels images) in about 5 min on an E5-2630 Intel processor workstation computer.

Appendix C: Multiview Deconvolution

Multiview deconvolution, more desirable than simple fusion procedures for precision and information preservation, becomes essential with multiview imaging for resolution improvement by increased isotropy of detection.[17,26] RL algorithm is already used to remove artifacts from light microscopy[37,38] and has proven appropriate and accurate for multiview deconvolution[23,26–28] even though computationally challenging. Without the use of beads, the efficient estimate of the point spread function (PSF) becomes challenging, especially when its shape varies for spatially inhomogeneous light-sheet depth. Variational deblurring,[39] although attractive, is still hardly applicable to large 3-D images for having detrimental memory and computational costs. Since we chose a large light-sheet depth and FOV, we consider a spatially homogeneous PSF designed with a Gaussian shape in which standard deviation $\sigma(z) = 11$ μm is related to the light-sheet depth (cf., main text Sec. 2.1). We set $\sigma(z) \simeq T/3$, so 95% of the light-sheet intensity Gaussian profile is recovered.

We used the RL iteration updates formulated in Ref. 26 and add a total variation (TV) regularization term yielding to

$$\varphi^{r+1} = \varphi^r \prod_{v \in V} \mathrm{TV}\left(\frac{\phi_v}{\varphi^r * P_v} * P_v^*\right), \qquad (6)$$

where φ^r is the deconvolved image at iteration r, ϕ_v is the original image view v, P_v is the PSF kernel corresponding to view v, P^* is the mirrored version of kernel P, * is the convolution operator, and the TV term is

$$\mathrm{TV}(I) = \left[1 - \lambda\, \mathrm{div}\left(\frac{\nabla_I}{|\nabla_I|}\right)\right]^{-1}, \qquad (7)$$

where λ is the regularization parameter, div() is the divergence operator, and ∇_I is the gradient of I.

RL deconvolution must be carefully parameterized regarding the three parameters known to mainly influence the convergence process. The PSF is, of course, the major one, but we cannot extract the PSF from beads. Furthermore, there is no geometrical optic model for the interaction between a sphere and planar sheet illumination, as opposed to other microscopy configurations such as confocal

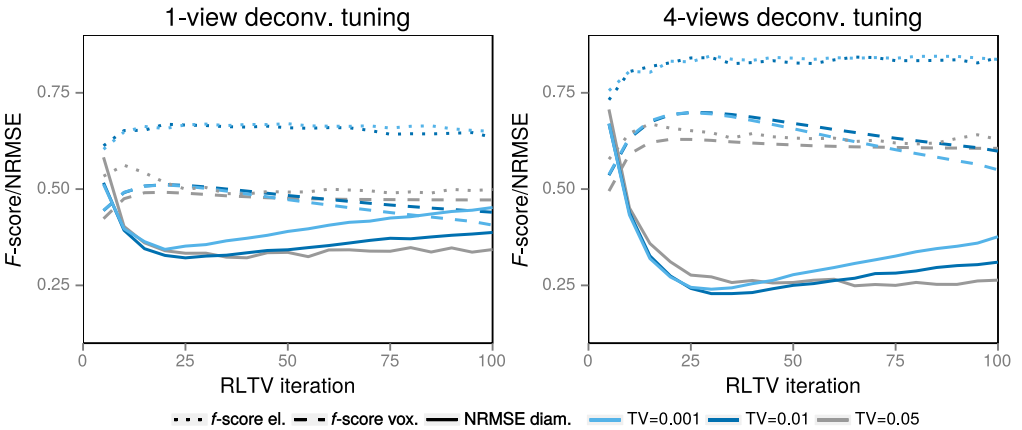

Fig. 7 Tuning the multiview RL deconvolution algorithm with TV regularization according to three accuracy metrics, using ground truth data set #1.

microscopy. For this reason, we empirically adjust the designed Gaussian-based PSF (see previous paragraph). We consider the influence of two supplementary parameters of the RL deconvolution: the number of iteration and the amplitude of the TV regularization term. We focus on the tuning process using the three low-level metrics previously described: the voxel matching, the segment-element matching, and the diameter error. Figure 7 shows these three metrics computed from ground truth data set #1, for one-view and four-views configurations. Optimal parameters are found to be very similar between one-view and four-views configurations, i.e., about 25 iterations with a TV term of about 0.001. However, an important relative difference is found between one view and four views up to 0.12 on voxels matching, 0.18 on element matching, and 0.1 on diameter error at the advantage of the four-views configuration.

Appendix D: Data Sets

Synthetic data have been generated from manual segmentation of three $128 \times 128 \times 128$ voxels images leading to sample #1, 2 and 3. Figure 8 illustrate various steps of the resulting segmentation and synthetic data obtained from sample #1.

Appendix E: Graph Similarity Measurement

Graph similarity uses the concept of intrinsic curvature of the graph embedding using its spectral properties.[35,40] Let us denote the graph $G = (V, E)$, where V is the set of nodes and E is the set of edges. The Laplacian matrix L of G is obtained from the adjacent matrix A and the degree diagonal matrix D by $L = D - A$, where $D(u, v) = \sum_{v \in V} A(u, v) = d_u$. The normalized Laplacian is $\hat{L} = D^{1/2} L D^{-1/2}$. The spectral decomposition is $\hat{L} = \Phi \lambda \Phi^{\mathrm{T}} = \sum_{i=1}^{|V|} \lambda_i \phi_i \phi_i^{\mathrm{T}}$, where λ_i is the i'th eigenvalue and ϕ_i is the i'th eigenvector. Using the heat kernel equation, we can defined the Euclidian distance between nodes u and v as

$$d^2(u, v) = \sum_{i \in |V|} \exp(-\lambda_i t)[\phi_i(u) - \phi_i(v)]^2. \tag{8}$$

The curvature associated with each edge is defined by $k^2(u, v) = 24[1 - d(u, v)]$.

We can then compute the similarity between graphs $G_1 = (V_1, E_1, k_1)$ and $G_2 = (V_2, E_2, k_2)$. The set of all nodes connected to the node $I \in G_2$ by an edge is defined as $C_I^2 = \{J | (I, J) \in E_2\}$, and the corresponding set of nodes connected to the node $i \in G_1$ by an edge is $C_i^1 = \{j | (i, j) \in E_1\}$.

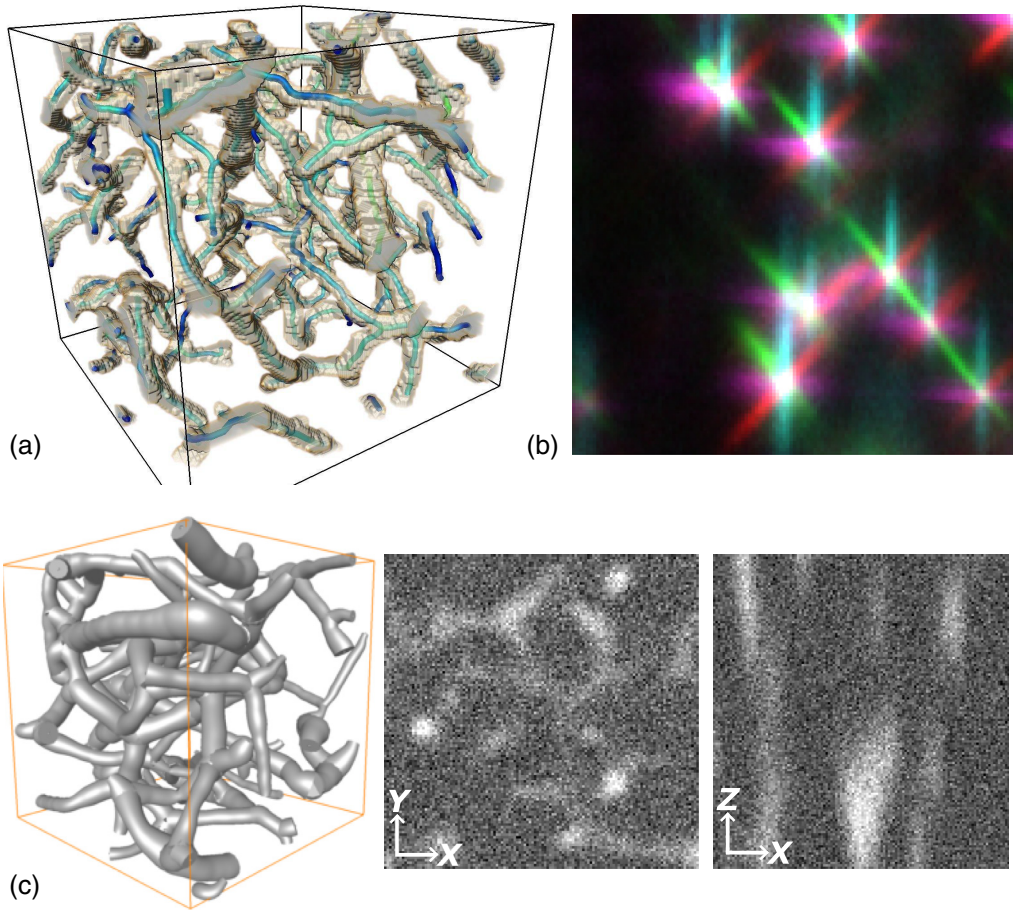

Fig. 8 (a) Ground truth data set #1 of $128 \times 128 \times 128$ μm^3 manually segmented; the vectorized graph network overlays the binary image. (b) Typical registration of four isotropic views in the *XZ*-plan (0 deg cyan, 45 deg red, −45 deg green, and 90 deg magenta). (c) Synthetic data set of $128 \times 128 \times 128$ μm^3: the 3-D graph network visualization (left) and the generated convolved image (middle and right) with additive Gaussian noise, PSNR = 40 dB.

The similarity measurement defined in Ref. 41 is finally given by

$$S(G_1, G_2) = \frac{1}{|V_1| \times |V_2|} \sum_{i \in V_1} \max_{I \in V_2} \sum_{j \in C_1^i} \max_{J \in C_I^2} P[(i,j) \rightarrow (I,J) | k^2_{(I,J)}, k^1_{(i,j)}]. \quad (9)$$

Appendix F: Flow Transport Model

The adopted discrete perfusion network is related to previously described flow microcirculation models[42–44] already used to model blood perfusion from image-based network extraction.[7–9] The basic assumptions of the modeling are related to the fact that, since fluid inertial effects are negligible in microcirculation flows, the relation between the pressure drop and the blood flux is linear. Furthermore, since the aspect ratio of the vessels, i.e., the ratio between average diameter and length, is small, the fluid flow through these elongated structures can be approximated using lubrication approximation, as detailed in Ref. 9. Such simplistic but robust modeling can also include the presence of red blood cells (RBC), by taking into account a supplementary pressure drop associated with their presence, through a saturation parameter (the volume fraction of RBC). In any case, since the pressure gradient is linearly varying along each vessel centerline, it can be integrated from each bifurcation to the next. Hence, it provides a single transport coefficient describing the proportionality between the pressure difference ΔP between two successive bifurcations and the flux Q arising in each vascular segment: $Q = K_h \Delta P$. This coefficient $K_h = -\pi/[128 \int \mu_a / D(s)^4 \mathrm{d}s]$ is related to the integration along the vessel length of the apparent viscosity of the blood μ_a and the vessel local diameter $D(s)$ varying along the vessel centerline curvilinear length s. Hence, from image-based skeletonization providing the local diameter of each vessel, one is able to build, for each vascular segment, the perfusion coefficient K_h. Then, applying flux conservation at each node permits solving for the pressure at each bifurcation.

Appendix G: Vascular Properties of Adipose Biological Tissue

Figure 9 illustrates the statistical results resulting from the complete vectorization of the micro-vascular network of a cubic millimeter of adipose tissue.

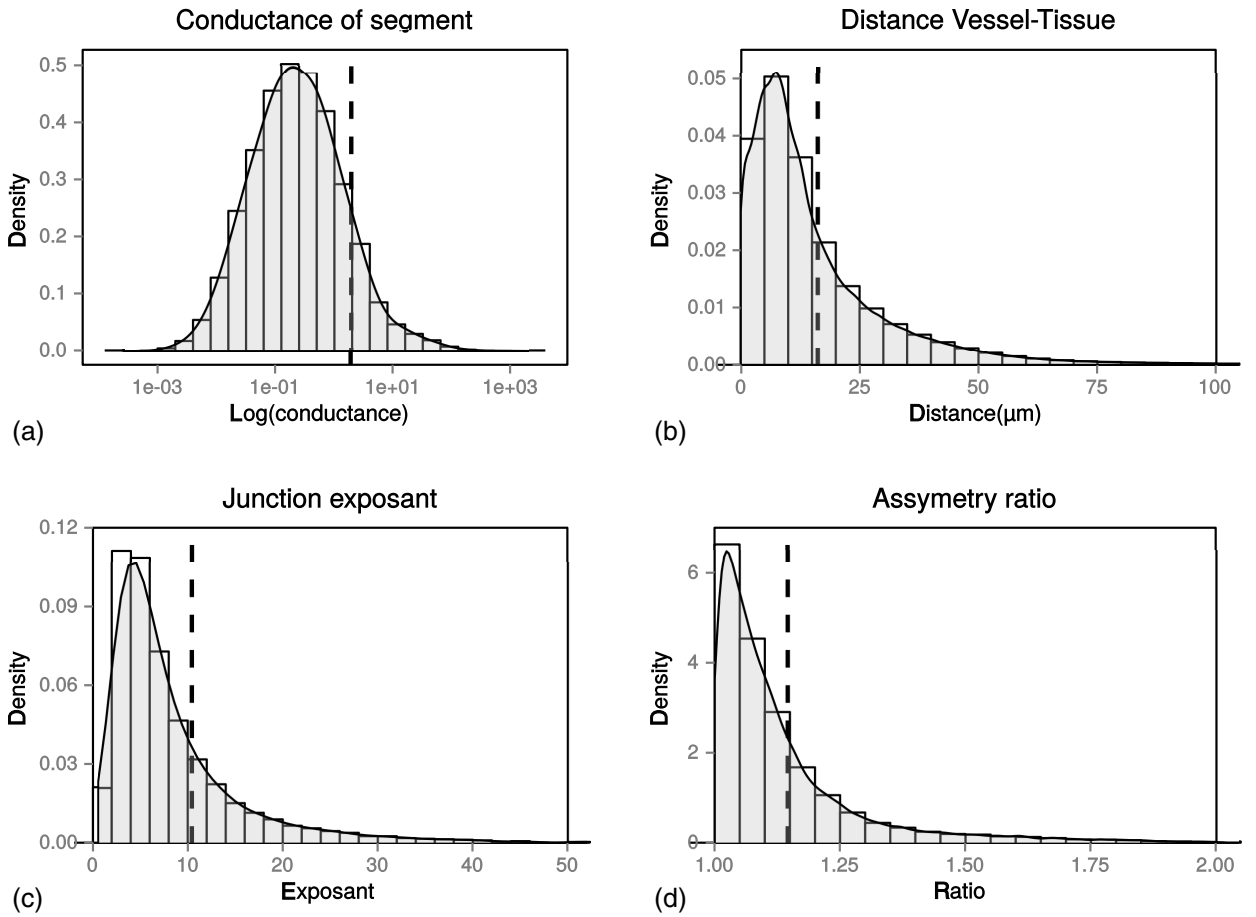

Fig. 9 Vascular network statistics extracted from the 1-mm^3 vascular network sample modelized from the inguinal adipose tissue in mice. (a) Conductances distribution, (b) distances vessel–tissue distribution: distances are obtained from the distance map calculated on the binary image, (c) junction exposants distribution, and (d) asymmetry ratio distribution.

Disclosures

The authors have no relevant financial interests in this paper and no potential conflicts of interest to disclose.

Acknowledgments

The authors thank J. Rouquette, L. Casteilla, A. Lorsignol, and C. Barreau for assistance with the imaging acquisition system and the mice preparation; L. Bardía for glass beads preparation; and P. Weiss, L. Risser, R. Guibert, and J. Dichamp for helpful discussions. This work was performed using HPC resources from CALMIP, Grant No. 2016-[P16050]. This work was supported by Region Occitanie, Grant No. 2016-[14050455].

References

1. H.-U. Dodt et al., "Ultramicroscopy: three-dimensional visualization of neuronal networks in the whole mouse brain," *Nat. Methods* **4**(4), 331–336 (2007).
2. B. Laviña and K. Gaengel, "New imaging methods and tools to study vascular biology," *Curr. Opin. Hematol.* **22**(3), 258–266 (2015).
3. A. Maizel et al., "High-resolution live imaging of plant growth in near physiological bright conditions using light sheet fluorescence microscopy," *Plant J.* **68**(2), 377–385 (2011).
4. R. Dickie et al., "Three-dimensional visualization of microvessel architecture of whole-mount tissue by confocal microscopy," *Microvasc. Res.* **72**(1–2), 20–26 (2006).
5. N. Jährling, K. Becker, and H.-U. Dodt, "3D-reconstruction of blood vessels by ultramicroscopy," *Organogenesis* **5**(4), 227–230 (2009).
6. M. Dobosz et al., "Multispectral fluorescence ultramicroscopy: three-dimensional visualization and automatic quantification of tumor morphology, drug penetration, and antiangiogenic treatment response," *Neoplasia* **16**(1), 1–13 (2014).
7. P. Blinder et al., "The cortical angiome: an interconnected vascular network with noncolumnar patterns of blood flow," *Nat. Neurosci.* **16**(7), 889–897 (2013).
8. J. Reichold et al., "Vascular graph model to simulate the cerebral blood flow in realistic vascular networks," *J. Cereb. Blood Flow Metab.* **29**(8), 1429–1443 (2009).
9. R. Guibert et al., "Cerebral blood flow modeling in primate cortex," *J. Cereb. Blood Flow Metab.* **30**(11), 1860–1873 (2010).
10. R. Guibert et al., "Coupling and robustness of intra-cortical vascular territories," *Neuroimage* **62**(1), 408–417 (2012).
11. F. Kirbas and C. Quek, "A review of vessel extraction techniques and algorithms," *Comput. Surv.* **36**(2), 81–121 (2004).
12. D. Lesage et al., "A review of 3D vessel lumen segmentation techniques: models, features and extraction schemes," *Med. Image Anal.* **13**(6), 819–845 (2009).
13. L. Risser et al., "From homogeneous to fractal normal and tumorous microvascular networks in the brain," *J. Cereb. Blood Flow Metab.* **27**, 293–303 (2007).
14. L. Risser et al., "A 3D-investigation shows that angiogenesis in primate cerebral cortex mainly occurs at capillary level," *Int. J. Dev. Neurosci.* **27**(2), 185–196 (2009).
15. J. Liu et al., "A dual role for ErbB2 signaling in cardiac trabeculation," *Development* **137**, 3867–3875 (2010).
16. S. Preibisch et al., "Software for bead-based registration of selective plane illumination microscopy data," *Nat. Methods* **7**(6), 418–419 (2010).
17. P. J. Verveer et al., "High-resolution three-dimensional imaging of large specimens with light sheet-based microscopy," *Nat. Methods* **4**(4), 311–313 (2007).
18. J. Mertz and J. Kim, "Scanning light-sheet microscopy in the whole mouse brain with HiLo background rejection," *J. Biomed. Opt.* **15**, 016027 (2017).
19. A. Masson et al., "High-resolution in-depth imaging of optically cleared thick samples using an adaptive SPIM," *Sci. Rep.* **5**, 1–14 (2015).
20. B. Berthet and A. Maizel, "Light sheet microscopy and live imaging of plants," *J. Microsc.* **263**(2), 158–164 (2016).
21. J. Lim et al., "Light sheet fluorescence microscopy (LSFM): past, present and future," *Analyst* **139**(19), 4758–4768 (2014).
22. R. Prevedel et al., "Simultaneous whole-animal 3D imaging of neuronal activity using light-field microscopy," *Nat. Methods* **11**(7), 727–730 (2014).
23. R. K. Chhetri et al., "Whole-animal functional and developmental imaging with isotropic spatial resolution," *Nat. Methods* **12**(12), 1171–1178 (2015).
24. A. Costa et al., "Calcium dynamics in root cells of Arabidopsis thaliana visualized with selective plane illumination microscopy," *PLoS One* **8**(10), e75646 (2013).
25. S. Klein et al., "Elastix: a toolbox for intensity-based medical image registration," *IEEE Trans. Med. Imaging* **29**(1), 196–205 (2010).
26. S. Preibisch et al., "Efficient Bayesian-based multiview deconvolution," *Nat. Methods* **11**(6), 645–648 (2014).
27. Y. Wu et al., "Spatially isotropic four-dimensional imaging with dual-view plane illumination microscopy," *Nat. Biotechnol.* **31**(11), 1032–1038 (2013).
28. B. Schmid and J. Huisken, "Real-time multi-view deconvolution," *Bioinformatics* **31**(20), 3398–3400 (2015).
29. L. Risser, F. Plouraboué, and X. Descombes, "Gap filling of 3-D microvascular networks by tensor voting," *IEEE Trans. Med. Imaging* **27**(5), 674–687 (2008).
30. K. Palágyi et al., "A sequential 3D thinning algorithm and its medical applications," *Lect. Notes Comput. Sci.* **26**, 409–415 (2001).
31. M. Schneider et al., "Joint 3-D vessel segmentation and centerline extraction using oblique Hough forests with steerable filters," *Med. Image Anal.* **19**(1), 220–249 (2015).
32. J. Krebs et al., "Robust non-rigid registration through agent-based action learning," *Lect. Notes Comput. Sci.* **10433**, 344–352 (2017).
33. Q. Dou et al., "3D deeply supervised network for automated segmentation of volumetric medical images," *Med. Image Anal.* **41**, 40–54 (2017).
34. C. Scott and R. Nowak, "Robust contour matching via assignment problem," *IEEE Trans. Image Process.* **15**(7), 1831–1838 (2006).
35. H. Elghawalby and E. R. Hancock, "Measuring graph similarity using spectral geometry," *Lect. Notes Comput. Sci.* **5112**, 517–526 (2008).
36. A. Robles-Kelly and E. R. Hancock, "A Riemannian approach to graph embedding," *Pattern Recognit.* **40**(3), 1042–1056 (2007).
37. M. Laasmaa, M. Vendelin, and P. Peterson, "Application of regularized Richardson–Lucy algorithm for deconvolution of confocal microscopy images," *J. Microsc.* **243**(2), 124–140 (2011).
38. N. Dey et al., "3D microscopy deconvolution using Richardson–Lucy algorithm with total variation regularization," Tech. Rep., INRIA (2004).
39. M. Temerinac-Ott et al., "Spatially-variant Lucy–Richardson deconvolution for multiview fusion of microscopical 3D images," in *IEEE Int. Symp. on Biomedical Imaging: From Nano to Macro*, pp. 899–904 (2011).
40. J. Huisken and D. Y. Stainier, "Selective plane illumination microscopy techniques in developmental biology," *Development* **136**, 1963–1975 (2009).
41. B. Huet and E. Hancock, "Relational object recognition from large structural libraries," *Pattern Recognit.* **35**, 1895–1915 (2002).
42. A. R. Pries, K. Ley, and P. Gaehtgens, "Generalization of the Fahraeus principle for microvessel networks," *Am. J. Physiol.* **251**, H1324–H1332 (1986).
43. A. R. Pries et al., "Blood flow in microvascular networks—experiments and simulation," *Circ. Res.* **67**, 826–834 (1990).
44. A. R. Pries, D. Neuhaus, and P. Gaehtgens, "Blood viscosity in tube flow: dependence on diameter and hematocrit," *Am. J. Physiol.* **263**, H1770–H1778 (1992).

Pol Kennel received his MSc degree in computer science from the University of Montpellier 2, France, in 2009. He completed his PhD in image analysis and remote sensing applied to ecology with International Center for Agronomic Research and Development (CIRAD), French Institute of Pondicherry (IFP), and the University of Montpellier 2, in November 2013 where he also taught computer science as an assistant professor. His research interests are texture analysis for images segmentation, remote sensing for ecological

applications, saliency analysis for cultural heritage, and biomedical image processing.

Lise Teyssedre: Biography is not available.

Julien Colombelli is the core facility manager of the advanced digital microscopy (ADM) platform at the IRB Barcelona, Spain.

Franck Plouraboué received his PhD in physics from the University of Paris 7, France, in 1996. He is research director at CNRS at the Fluid Mechanics Institute of Toulouse IMFT UMR 5502. His research interests are covering microhydrodynamics, applied mathematics, and biomodeling and imaging.